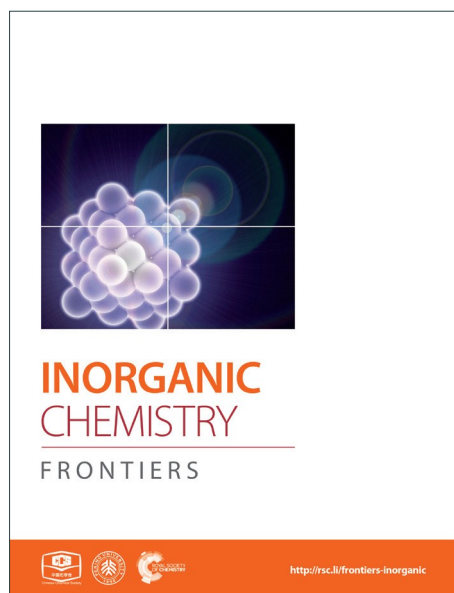
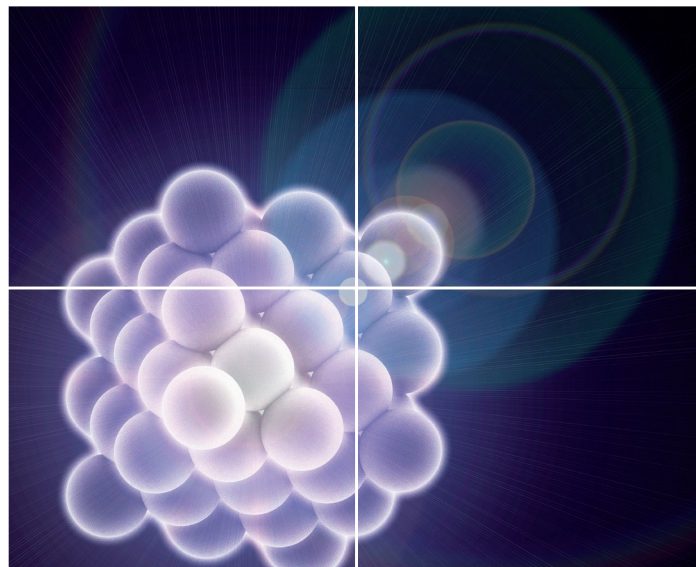


INORGANIC CHEMISTRY

FRONTIERS

Accepted Manuscript



This is an *Accepted Manuscript*, which has been through the Royal Society of Chemistry peer review process and has been accepted for publication.

Accepted Manuscripts are published online shortly after acceptance, before technical editing, formatting and proof reading. Using this free service, authors can make their results available to the community, in citable form, before we publish the edited article. We will replace this *Accepted Manuscript* with the edited and formatted *Advance Article* as soon as it is available.

You can find more information about *Accepted Manuscripts* in the [Information for Authors](#).

Please note that technical editing may introduce minor changes to the text and/or graphics, which may alter content. The journal's standard [Terms & Conditions](#) and the [Ethical guidelines](#) still apply. In no event shall the Royal Society of Chemistry be held responsible for any errors or omissions in this *Accepted Manuscript* or any consequences arising from the use of any information it contains.

**Nanocrystalline iron oxide based electroactive materials in lithium ion batteries:
The critical role of crystallite size, morphology, and electrode heterostructure
on battery relevant electrochemistry**

Andrea M. Bruck^{a,‡}, Christina A. Cama^{a,‡}, Cara N. Gannett^{b,c},

Amy C. Marschilok^{a,d,*}, Esther S. Takeuchi^{a,d,e,*}, Kenneth J. Takeuchi^{a,d,*}

- a. Department of Chemistry, Stony Brook University, Stony Brook, NY 11794
- b. Department of Chemistry, State University of New York at Geneseo, Geneseo, NY 14454
- c. Center for Inclusive Education, Stony Brook University, Stony Brook, NY 11794
- d. Department of Materials Science and Engineering, Stony Brook University, Stony Brook, NY 11794
- e. Energy Sciences Directorate, Brookhaven National Laboratory, Upton, NY 11973

*corresponding authors: (ACM) amy.marschilok@stonybrook.edu, (EST) esther.takeuchi@stonybrook.edu, (KJT) kenneth.takeuchi.1@stonybrook.edu

[‡]AMB and CAC contributed equally to the manuscript.

Abstract

For the rational design and development of new active material for energy storage, the importance of crystallite size control and direct synthesis of materials with desirable properties is broadly applicable. Recently, the use of nanoparticles and crystallite size control has redefined electrode design strategies, due in part to the large surface area / volume ratios providing more pathways for ion movement within the bulk electrode. This review is structured primarily as a case study, where reports involving a specific densely structured iron oxide, magnetite, Fe₃O₄, and its use as an electrode in LIBs are used as examples. Due to the high theoretical capacity

(924 mAh/g), and opportunity for implementation of a low cost electrode material, magnetite was selected as the model material for this review. Notably, crystallite size, morphology, and electrode heterostructure can all play a critical role in battery relevant electrochemistry, particularly for crystallographically dense materials such as Fe_3O_4 . Several examples of Fe_3O_4 based composites are described, incorporating different types of conductive materials such as carbons as part of the structure. Additionally, this review also provides a brief introduction to a newer iron oxide based material with a 2D layered structure, silver ferrite, where crystallite size control was synthetically achieved. By focusing on two specific iron oxide based nanoscale inorganic materials, this review highlights and distinguishes the contributions of electroactive material crystallite size, morphology and electrode heterostructure to electrochemical behavior, facilitating the future development of next generation of battery electrodes.

1. Introduction

Non-renewable energy is being consumed at a high enough rate to warrant a modern strategy for managing the remaining energy stores. Towards this end, a key component of the efficient generation and use of energy is energy storage. While there are a variety of energy storage technologies, batteries are a promising solution for both stationary and mobile applications, because both the chemistries and the engineering of batteries can be adjusted to suit the application, and historically batteries have enabled a number of devices. However, critical applications such as electric grid re-design and totally electric vehicles await batteries which can fulfill both energy and safety requirements.

Historically, aqueous-electrolyte batteries were prevalent as consumer batteries, but were limited to 1.5 V. Non-aqueous batteries were then introduced because they offered high voltages and larger capacities. Further improvement of the non-aqueous-electrolyte batteries led to the development of the lithium-ion battery (LIB) - first prototyped in 1986.¹ Yoshino from the Asahi Kasei Corporation was the first to create a $\text{Li}_{1-x}\text{CoO}_2/\text{C}$ cell,¹ which employed a transition-metal oxide electrode, a carbonaceous electrode, and a non-aqueous lithium ion-based electrolyte. In 1991, the LIB was first commercialized by SONY, initially used for camcorders and cell

phones, featuring twice the energy density of prior batteries which had a profound impact on the portable electronics market.^{2,1}

Applications of LIBs have seen a dramatic growth because of its high capacity, high discharge voltage, and cycle durability. The electrochemical performance of LIB systems is continually being optimized for consumer use with no indication of retracting as shown by **Figure 1**. Research focuses on improvements to these batteries systems such as maximizing the power density by improving both the voltage and capacity. This capability is necessary to satisfy the current interest in hybrid and electric vehicles (EVs) which require a high power energy source to function. LIBs have shown the greatest promise for EVs but still require increased power and energy density to compete with current fossil fuel sources.³ Much of LIB science and technology research has focused on the individual components of the LIB, including the anode, cathode, electrolyte, and separator. Anode research has centered on graphite-based materials, metallic alloys, intermetallics, as well as Li metal, where each strategy is rooted in specific desirable material attributes.^{4,5} Cathode research has involved the synthesis and electrochemistry of new materials, many being metal oxides.^{6,7} This section provides a brief history of inorganic electroactive materials developments significant to the introduction of LIB, followed by a discussion of materials parameters which form the subsequent sections of this review. While many parameters can affect the performance of lithium battery active materials, such as the electrolyte composition,⁸⁻¹⁰ active material surface area,¹¹ and parasitic reactions including active material dissolution¹²⁻¹⁴ and surface film formation,¹⁵ the bulk of this review is focused on the key contributions of electroactive material crystallite size, morphology and electrode heterostructure to electrochemical behavior.

In general, LIB research has been inspired by the first $\text{Li}_{1-x}\text{CoO}_2/\text{C}$ cell. Since its introduction by Goodenough and coworkers in 1980, LiCoO_2 remains a commonly used cathode material in lithium ion batteries¹⁶. With the desire to create a lower cost material while maintaining the success seen by LiCoO_2 , an interest in nickel based lithium oxides developed due to the isostructural properties of the analogous materials. A family of materials, $\text{Li}[\text{Ni}_{1-x}\text{Co}_x]\text{O}_2$, was first studied by Delmas and coworkers.¹⁷ Subsequently, a group of layered $\text{Li}[\text{Ni}_{1-x-y}\text{Co}_x\text{Mn}_y]\text{O}_2$ compounds demonstrated good capacity retention and high discharge rates.^{6, 18}

As LIB research progressed, metal oxides from several structural families were studied as LIB cathode materials, including spinel (LiM_2O_4) and olivine (LiMPO_4), as well as other layered compounds (LiMO_2). Recently, intercalation materials including silicates (Li_2MSiO_4), borates (LiMBO_3), and fluorides (LiMPO_4F) were studied as cathode materials.¹⁹ Concomitant with an expansion of the range of materials studied, concepts such as surface structure and variation in composition of materials have become increasingly important in battery research.²⁰ Specifically, surface versus interior material differences for properties such as ion insertion and electrical conductivity may prove critical towards understanding fundamental battery chemistry and the rational development of new battery technologies.

At the turn of the 21st century, metal oxide based anodes were reported to produce more than twice the capacity of traditional carbon electrodes upon full utilization. At that time, LIB anodes contained carbon materials coupled with these metal oxides, with metal oxide crystallite sizes in the micrometer range. Impressive capacities were achieved through full reduction of the metal oxide with the formation of metal nanoparticles during the discharge process.²¹ After this discovery, research in batteries for both anodes and cathodes turned to uncovering the properties of nanoparticles relevant to electrical energy storage.

The use of nanoparticles redefined electrode design strategies, due in part to the large surface area / volume ratios providing more pathways for ion movement within the bulk electrode. Further, nanomaterials reduced the path length of ion movement within an individual crystal, thus, reducing the resistance to Li^+ diffusion into the interior of the crystal of an electrode material,³ and a more facile lithium transport within the bulk electrode.²⁰ This is a promising feature of nanomaterials in LIBs; facile discharging and charging results in greater power opportunities, shorter charging times, less heat generation and greater capacities under load – desirable properties for all battery applications, but especially for portable applications such as electric vehicles. Finally, by synthetically manipulating the morphology and porosity of the nanomaterials, the above effects can be mitigated or enhanced.

Combining two or more materials within an electrode to generate a composite electrode provides an opportunity to address multiple issues simultaneously. Composite electrodes can be prepared by a variety of strategies, including: 1) mixing the various components, 2) coating one material with another in a core-shell strategy, 3) layering materials using techniques such as

chemical vapor deposition or atomic layer deposition, or 4) developing synthetic strategies where composite materials are formed *in-situ*.²²⁻²⁵ Historically, an important goal for composite electrodes was enhanced electrical conductivity, attained by mixing electrically conductive carbon materials with less conductive electroactive materials. The sizes and morphologies of the electroactive particles and carbon particles can determine the optimal amount of carbon to be used to address electrical conductivity. From percolation theory, the carbon particles should be much smaller than the electroactive particles, to enhance electrical conductivity and facilitate Li⁺ transport. In practice, the size, morphology and phase of the carbon particles are variable, and variety of carbon particles have been used as additives. Notably, semiconducting and conducting polymers such as polypyrrole and polyaniline have shown to be effective in raising rate capabilities and therefore cathode performance by increasing electrical conductivity without significant decrease in lithium ion flow.⁷

This review is structured primarily as a case study, where reports involving a specific iron oxide, magnetite, Fe₃O₄, and its use as an electrode in LIBs are used as examples. As magnetite has a densely packed inverse spinel structure, the use of nanoscale materials and synthetic crystallite size control are particularly important. However, the importance of crystallite size control and direct synthesis of materials with desirable properties is broadly applicable. Therefore, this review also provides an introduction to a newer material with a 2D layered structure, silver ferrite, where crystallite size control was synthetically achieved. Further, the silver ferrite material is synthesized as a nanocomposite, consisting of silver ferrite and maghemite. Due to the newness of these materials, the battery-relevant literature is limited, thus the two introductions in this review represent new strategies towards future structure/function studies involving battery-relevant electrochemistry. In all cases, the role of crystallite size proved to significantly impact electrochemical behavior, a paradigm for the next generation of batteries.

2. Material properties and resulting electrochemistry of magnetite

Lithiation of magnetite

Magnetite is a naturally occurring mineral found in the earth's crust; therefore, it is abundant, environmentally friendly, cheap, and non-toxic. Magnetite is also easy to synthesize and can be prepared through simple, non-hazardous techniques such as through a facile aqueous co-precipitation method. Complete reduction of magnetite involves the transfer of 8 electrons, providing opportunity for an impressive capacity of 925 mAh/g.²⁶ Magnetite assumes a cubic inverse spinel structure with a space group of $Fd\bar{3}m$. The formula of magnetite can be written as $Fe^{2+}Fe^{3+}_2O_4$,²⁷ where the unit cell contains eight Fe^{2+} cations in octahedral sites and sixteen Fe^{3+} cations, distributed evenly among the tetrahedral sites and the octahedral sites as shown in **Figure 2**. The oxygen anions form layers parallel to 111 in a cubic close-packed arrangement.

Lithiation of magnetite first forms $Li_xFe_3O_4$, where $x = 2$.²⁸ Upon further lithiation, $Li_xFe_3O_4$ is formed, where $x = 2-5$. However, in this step, Thackeray and Goodenough first proposed that the iron cations in the tetrahedral sites of Fe_3O_4 are displaced by lithium ions in a cooperative displacement reaction,²⁹ where a rock salt-type structure is formed with a lattice constant of 8.47 Å³⁰. The iron ions move into octahedral sites during this displacement.²⁸ As the reduction progresses, Li_2O becomes displaced from the lattice and Fe metal is formed which has a body-centered cubic structure. The structural change that occurs when the rock salt is changed to iron metal has been proposed to be at least partially reversible.³⁰ Notably, the initial reactions are insertion reactions where the lithium ion can insert into the Fe_3O_4 structure with minimal structural distortion, while upon further reduction, a conversion reaction occurs generating Fe metal and Li_2O as products of full discharge.

Notably, achieving full conversion and complete utilization of the electroactive metal centers can be challenging for crystallographically dense materials such as Fe_3O_4 . These densely structured materials do not have well defined layers or tunnels for facile lithium ion insertion. Conceptually, it can be envisioned that electrochemical lithiation would proceed from the surface to the interior, which could be visualized as a shrinking core of magnetite surrounded by reduced or partially reduced surface.³¹ This could affect the functional capacity of these systems due to polarization resulting from kinetic limitations such as slow lithium ion diffusion.³² These systems in particular would significantly benefit from nanosized materials with increased surface area to volume ratios, as discussed in the next section.

Crystallite size effects on magnetite's electrochemical performance

In 2008, Komaba et. al. compared the electrochemical performance of magnetite particles that were 400, 100 and 10 nm in size. There was no significant reactivity observed in the 400 nm systems; however, the 100 and 10 nm systems reached initial discharge capacities of 70 mAh/g and 130 mAh/g after discharging to 1.5V at 20 mA/g, respectively. After 30 cycles, the capacity still delivered 96 mAh/g which was attributed to the improved performance of the nano-sized sample.³³

The nano-size effect describes the change in properties of nanoscale materials from their corresponding bulk form. As the size of a crystallite decreases, the surface area increases, thus increasing the surface area – to – volume ratio of the solid. The small size can also improve kinetics since Li^+ ion diffusion pathways can take place at smaller distances in nanoscale materials. Thus, decreasing the crystallite size can enhance capacity retention and coulombic efficiency. Despite all of these advantages, working on the nanoscale does have several challenges. For example, due to the large surface area, the nanocrystals can experience side reactions with the electrolyte. These side reactions often cause large irreversible capacity loss. Nanocrystals also have high surface energy due to the incomplete bonding at the surface. To accommodate the high surface energy, nanocrystals tend to aggregate. Aggregation can be detrimental to battery performance as it disrupts the conductive pathways within the cathode, thus causing poor efficiency and capacity retention. It is the aim of battery researchers to overcome these challenges associated with nanomaterials to enhance battery performance.

Various studies in the Takeuchi group have evaluated the $\text{Li}/\text{Fe}_3\text{O}_4$ system and have studied the nano-size effect at over a smaller size range and lower voltages than the Komaba studies.^{33, 34} Magnetite particles from 6 to 11 nm were successfully synthesized through a novel co – precipitation technique that varied concentration of the starting materials using triethylamine as a reagent.^{26, 35-38} The $\text{Li}/\text{Fe}_3\text{O}_4$ half cells were discharged at constant current between 3.0 and 1.0 V. As crystallite size decreased, the discharge capacity increased by 30 – 200%.³⁵

A closer look at the discharge profiles of different crystallite sizes of magnetite indicates significant differences in the smoothness of the voltage curves with varying crystallite size, as shown in **Figure 3**. Discharge slopes are smoother for the smaller crystallite sizes; however, the larger crystallite size sample exhibits a distinct plateau. Depending on the application, a flat

voltage profile with a distinguishable plateau providing more constant energy delivery may be more desirable. The discharge profile is influenced by the large quantity of surface defects present in the nanocrystalline magnetite. These surface defects cause a reduction in the band gap; thus, as Li^+ ions are inserting into the magnetite structure, the Fermi energy is gradually changing, rather than abruptly changing as it would in the bulk sample.³⁹

Saturation magnetization and XAS measurements are useful tools to determine the average oxidation state of materials. Bulk magnetite has a magnetization saturation of about 90 emu/g, which is higher than the saturation magnetization values for the co-precipitated magnetite.³⁶ Consistent with prior reports,⁴⁰⁻⁴³ the saturation magnetization decreased as crystallite size decreased for nanosized Fe_3O_4 , indicating the presence of excess Fe^{3+} in the smaller crystallite size magnetite. The XAS results in **Figure 4** show bulk magnetite samples with crystallite sizes of 26 nm to have lower pre-edge energies than the 8-10 nm co-precipitation prepared samples, consistent with a higher concentration of Fe^{3+} in the co-precipitation prepared samples,³⁷ as seen in other studies of nanocrystallite magnetite.⁴⁴ The saturation magnetization and XAS measurements are both consistent with the assumption of oxidized Fe^{3+} rich layer on the surface of the Fe_3O_4 nanoparticles, where the smaller crystallite size materials have a higher average oxidation iron oxidation state due to a larger surface area to volume ratio. While an increase in average iron oxidation state would increase the theoretical capacity of the material, calculations predict only ~10% increase based on the XAS results. Thus, the achieved 40-200% increase in capacity as a function of crystallite size cannot be explained solely by differences in iron oxidation state.

In order to gain additional insight regarding the discharge mechanism of magnetite, a combination of x-ray absorption spectroscopy and x-ray diffraction was used to determine structural changes as a function of electrochemical reduction for Fe_3O_4 of differing crystallite size (9 – 26 nm).²⁶ At the onset of electrochemical reduction through 1.7 electron equivalents of discharge, the reduced materials were consistent with a spinel like $\text{Li}_x\text{Fe}_3\text{O}_4$ local structure with iron ions in both tetrahedral and octahedral environments. Between 2.8 and 4.0 electron equivalents, a rock-salt phase was observed. Further reduction at 6.0 and 8.0 electron equivalents provided XAS consistent with Fe^0 nanoparticle formation, for the smaller crystallite sized material ≤ 11 nm. Notably, controlling the crystallite size of the Fe_3O_4 parent material was

key to obtaining this first direct empirical evidence of metallic Fe^0 formation upon full electrochemical reduction.

The larger surface area of nanoscale materials often causes a high degree of agglomeration, where particle size can be dependent on crystallite size.³⁶ Active material aggregation can contribute to increased charge transfer resistance for the electrode. Recently, the relationship between Fe_3O_4 crystallite size, Fe_3O_4 agglomerate size within a battery electrode, and electrochemical performance of Li/ Fe_3O_4 cells was investigated using TEM, Transmission X-ray microscopy (TXM) and x-ray absorption near – edge spectroscopy (XANES).³⁸ TEM results indicated the agglomerate size within processed electrodes containing 8 nm and 28 nm Fe_3O_4 was the same, as shown in **Figure 5a**. Despite the similar degrees of agglomeration, electrodes containing the smaller crystallite size material delivered ~20-200% higher specific energy, with the larger differences apparent under higher rate discharge. TXM-XANES data indicated that electrodes containing the 8 nm material discharged more evenly than those with the 28 nm material, **Figure 5b**, consistent with higher utilization for the smaller crystallite size material.

The voltage changes occurring within magnetite electrodes during discharge and open circuit voltage recovery were analyzed through a comparison of the mass transport time-constants associated with different length-scales within the electrode.³² Development of an effective multi-scale mathematical performance model required inclusion of both crystallite size and agglomerate size, indicating that both factors were significant to the mass transport process.³¹ Notably, even a small number fraction (<10%) of large Fe_3O_4 aggregates can have a significant impact on delivered capacity.

Magnetite of different morphologies

Magnetite of several types of morphologies from spheres to hollow spheres have been synthesized. **Table 1** provides a summary of the electrochemical behavior of magnetite of different morphological forms. Of the morphologies studied, hollow spheres seem to achieve the best performance. In the hollow sphere morphology, magnetite nanoparticles are clustered around empty space. The hollow sphere morphology alleviates the stress caused by volume changes during the conversion mechanism. Furthermore, the hollow sphere is composed of

nanoparticles which retain a small diffusion pathway for Li – ion, thus continuing to provide improved kinetics.⁴⁵⁻⁴⁷

There are different ways to prepare magnetite hollow spheres. In one reference, the hollow spheres were synthesized by hydrolyzing a solution of FeCl₃ in the presence of polyvinylpyrrolidone (PVP) at 200°C. As the Fe₃O₄ forms, the crystals begin to aggregate. The PVP stabilizes the surface of the crystallites and acts a nucleation site. It is suggested that Ostwald ripening causes the inner crystallites to dissolve and reform on the surface of the outer coated crystallites, thus forming a void in the center of the aggregate. SEM images show that the hollow microspheres are composed of nanoparticles between 30 and 40 nm with surface area of 12 m²/g. The material was tested against Li/Li⁺ and exhibited less polarization and better reversibility than the solid Fe₃O₄ microspheres. Furthermore, the hollow spheres achieved 40% higher capacity and better rate capability than the solid spheres. Electrochemical impedance spectroscopy experiments further suggested that the hollow sphere morphology reduces the charge – transfer resistance, thereby facilitating the transfer of Li⁺ ions.⁴⁶

The hollow sphere morphology can also be formed by other morphologies such as nanosheets.⁴⁵ These hollow spheres exhibited a high initial capacity of 1614 mAh/g and retained 65% of the initial capacity after 100 cycles at 500 mA/g. The solid spheres exhibited about 800 mAh/g capacity, thus, higher capacity was achieved by the hollow morphology. Further testing showed that at different rates the hollow morphology achieved higher capacities than the solid spheres. EIS experiments provided further evidence suggesting that the hollow spheres decrease the resistance more than the solid spheres.

Another technique that has been used to prepare hollow spheres is through ionic adsorption of magnetite nanoparticles to a hydrogel such as poly (methacrylic acid – co – ethylene glycol dimethacrylate) (poly(MMA/EGDMA)). The hollow morphology is achieved after annealing the sample at 500°C to remove the hydrogel. The hollow spheres were composed of Fe₃O₄ nanoparticles ranging in size from 10 – 100 nm according to SEM images. Compared to Fe₃O₄ nanoparticles, the hollow spheres exhibited better capacity retention over 35 cycles such that the nanoparticles and hollow spheres lost 67% and 12% of their initial capacity, respectively.⁴⁷

Other studies have prepared magneite nanoparticles which exhibit different shapes such as octahedra and hexahedra.^{48, 49} A low temperature hydrothermal synthesis was used to synthesize polyhedra which exhibited the different facets (010), (111), (110), (011), (11 $\bar{1}$), ($\bar{1}$ 11), ($\bar{1}$ 01), (001), (101), (100), and (0 $\bar{1}$ 1). This morphology exhibited better performance than the octahedra⁴⁹ and hexahedra⁴⁹ synthesized, as summarized in **Table 1**. After 50 cycles, the polyhedra nanoparticles achieved capacities of about 1100, 800, 600, and 400 mAh/g at current rates of 50, 100, 400, and 1000 mA/g, respectively.⁴⁸

These studies suggest that through manipulation of both crystallite size and morphology, electrochemical performance can be significantly improved and altered. Hollow spheres appear to offer the best morphology since that structure facilitates ion transfer as well as the reducing strain produced by the volume change experienced during the conversion reaction of Fe₃O₄ to Fe⁰. These features result in higher capacities during cycling at both high and low rates.

3. Electrochemistry of magnetite containing electrode heterostructures

Although magnetite is a semiconductor it is commonly studied combined with an electrically conductive carbon thus enhancing the electronic conductivity of the electrode.⁵⁰ Carbons of various type have been employed, including carbon black (CB), acetylene black (AB), Super P (SP), graphite, and carbon nanotubes (CNTs). Varying the carbon additive can have profound effects on the electrochemical properties of these electrode systems. For example, a recent study by Deng et. al. involved the effects of AB, SP, CNTs and a mixture of AB plus CNTs on the electrochemical performance of magnetite. Notably, a mixture of AB and CNTs provides increased rate capability, larger specific capacity after 30 cycles, and a lower impedance that overall maximizes the performance of the magnetite electrode in a LIB.⁵¹ Interest in composite electrodes such as electrically conductive materials plus redox electroactive material has inspired other studies in nanostructured materials and their effect on composite electrode electrochemistry. When carbon is employed as an electrically conductive material in a composite electrode, particularly those discharged under low voltage, it is important to consider the following reaction: $6C + Li \rightarrow LiC_6$ in capacity measurements.

Research in magnetite electrodes has included carbon nanostructures and magnetite nanostructures in a variety of LIB composite electrodes. One research strategy is to investigate

carbon materials such as CB or graphene which may yield a higher theoretical capacity than conventional carbon additives (372 mAh/g). There are two common approaches for this strategy (1) change the structure of magnetite on the nanoscale then use carbon as a coating or additive, or (2) use a carbon nanostructure such as graphene or graphene oxide as an anode material then deposit magnetite nanoparticles on their surface. In general, combinations of magnetite morphology, magnetite crystallite size, and a variety of carbon additives have been studied to optimize magnetite performance as an LIB electrode.

Studies of magnetite nanostructures where carbon was incorporated into the synthesis and used to promote electronic conductivity are summarized in **Table 2**. The morphology, crystallite size of magnetite, and weight percent of magnetite in the active electrode material was provided where reported. The mixture of active material and additional carbon additive was also provided where reported with the identification of the carbon type used. The initial and final capacities reported are also tabulated. Details from a subset of these studies are provided below, to illustrate unique or representative syntheses and electrochemistry results.

As magnetite electrodes utilize carbon additives to enhance electronic conductivity, there have been many investigations on optimizing the carbon material's structure, **Table 2**. A recent approach has been to use two-dimensional, single-atom thick, hexagonally arranged graphene sheets with the additional benefit that their rigid sp^2 hybridized structure reduces agglomeration of the magnetite nanoparticles.⁵² The most common synthetic approach starts with graphite and turns it to graphene oxide (GO) using a modified Hummers method. Using microwave techniques or an ultrasonic suspension an Fe^{3+} species is added to the GO and incorporated into the graphene matrix by forming Fe-O-C bonds as shown in **Figure 6a**. Zhang et. al reported having magnetite incorporated with polyethylenimine to hold a slightly positive charge and graphene with poly(sodium 4-styrenesulfonate) to hold a slightly negative charge where the electrostatic attraction holds the materials together. The Fe_3O_4 -graphene paper-like material isolated from the preparation showed impressive capacity (1140 mAh/g) for 220 cycles.⁵² Another study that added 20 nm magnetite particles on graphene nanosheets with a pore size around 3 nm via sonication reported a retained capacity of 1243 mAh/g for 50 cycles when cycled at a 0.2 A/g rate.⁵³ Others reported magnetite nanoparticles on graphene sheets providing between 500-650 mAh/g after 50 cycles under rates of $\sim 1A/g$.⁵⁴⁻⁵⁷

Another study reported magnetite dispersed on a graphite oxide nanosheet with no binder or carbon conducting additive synthesized using a modified Hummers method. Microwave irradiation was used to disperse an Fe^{3+} species and the graphite oxide which was then chemically reduced. This study showed that varying electrolyte from DEC to DMC had significant effect on the capacity retention of the material. The best performance with DEC provided 994 mAh/g after 50 cycles.⁵⁸

Zhao et. al developed a new method to modify the structure of the nanosheet by developing GO nanoscrolls with magnetite embedded on the interior by cold quenching GO sheets in liquid nitrogen. Three different wrapping structures were studied with the best electrochemical result showing a capacity of 1010 mAh/g after 50 cycles, similar to the nanosheets.⁵⁹ Another variation of the nanosheets is the assembly of a flower-like structure 3-5 microns across with pedals 60-90 nm thick and approximately 1 micron long. These flower-like materials provided a capacity of 1449 mAh/g after 49 cycles.⁶⁰ Similar studies were conducted with magnetite/GO composites consisting of nanoparticles between 10-20 nm crystallite size where magnetite represented 40-55% of the active material in the electrode, giving sustained capacities of 674 mAh/g.^{61, 62}

Three dimensional structures such as foams and carbon matrices have also been gaining interest in recent years. A study by Hu et. al used nickel foam cut into disks and annealed under hydrogen gas in a quartz tube with small amount of methane used for the graphene matrix, the mixture was cooled to room temperature and finally nitric acid was used to remove excess nickel metal resulting in a graphene foam. The graphene foam, a Fe^{3+} source, and carbon dioxide were added to a high pressure vessel resulting in the formation of graphene sheets with magnetite particles on the surface. Good reversibility of the foam structure was achieved as illustrated by the capacity of 924 mAh/g for 500 cycles, the highest cycle number reported on **Table 2**.⁶³

Other carbon foams with magnetite particles incorporated into their structure have been tested for their performance as electrode materials with varying results. In a study by Kang et. al, they synthesized a mesocellular foam and added the magnetite particles into the cells then studied Al_2O_3 's effect on the material to further stabilize the SEI layer. Their results showed that Al_2O_3 did aid in side reactions caused at the SEI, but this material still showed considerable fade from 1007 to 533 mAh/g after 150 cycles.⁶⁴ A more successful capacity retention of carbon

foam materials was reported by Wu et. al by drying a gelatin doped with an Fe^{3+} species that was annealed to produce the porous carbon foam with the magnetite nanoparticles. This foam retained a higher capacity of 1008 mAh/g over 400 cycles.⁶⁵

Other forms of carbon matrixes have been derived by synthesizing FeOOH nanoparticles, coating them in alcohol, then carbonizing in vacuum to produce an agglomeration of particles connected by the carbon residue, similar to the porous nanospheres previously mentioned. These batteries were constructed without any additional carbon added and still demonstrated a capacity of 777 mAh/g after 30 cycles.⁶⁶ Another study embedded magnetite nanoparticles (~5 nm) on CNT's with magnetite representing 41 wt% of the active material, then they used 10% AB as a conductive additive and 10% PVDF binder for their electrode and to found a capacity only slightly higher than graphite after 75 cycles.⁶⁷

One synthetic technique for generating Fe_3O_4 based nanostructures is the arc-discharge method. Fe metal is used as the anode and carbon needle as the cathode, the chamber is filled with Ar and H_2 then ethanol is introduced and held at a precise pressure for 24 hours resulting in 30-60 nm magnetite nanoparticles with an onion-like carbon coating. The "onion-like" layering is attributed to the defects in the collapsed graphite layer. These defects seemed to accommodate the volume changes during the lithiation/delithiation process and provided high coulombic efficiency (~86% after 300 cycles).⁶⁸ A more typical synthesis for nanoparticles is a simple one or two step wet chemical synthesis with an iron oxide precursor isolated. A carbon source can be added (such as sucrose, polymerized dopamine, etc) or sourced from residual hydrocarbons from synthesis. The resulting particles are then subjected to heat well over combustion of the carbon source and resulting in formation of core-shell structures as depicted conceptually in **Figure 6b**. Enhanced capacity, improved cycling capability, and a significant decrease in AC impedance for magnetite based electrodes in both lithium and sodium batteries have been reported as a result of the core-shell synthesis approach.⁶⁹⁻⁷² Frequently, the core-shell Fe_3O_4 material is combined with another conductive carbon to generate the composite electrode. For example, Park and Myung prepared core-shell nanoparticles where the core magnetite is 10-100 nm and the shell is approximately 1-10 nm and deposited them onto two-dimensional carbon nanotubes.⁷² Different types of Fe_3O_4 morphologies have been achieved in concert with core-shell synthesis. For example, in a synthesis reported by Xia et. al Fe_2O_3 nanotubes were

generated then heated above 400°C for 3 h in inert atmosphere to produce magnetite nanotubes. Glucose was added as a carbon source during synthesis then degraded to a carbon coating producing a core-shell nanotube 200-300 nm long with walls 10-20 nm in thickness. These materials exceeded the capacity of graphite, attributed to shortening of the Li^+ ion diffusion path length.⁷³

A similar synthesis was used to generate a 200 nm magnetite nanorods from FeOOH nanorods also using glucose as a carbon source. These rods are similar to the nanotubes but lack the hollow structure in the center but still exhibit comparable initial capacity and fade.⁷⁴ A magnetite core-carbon shell nanorod was prepared by Liu et. al using Fe_2O_3 nanorods and citric acid as reagents.⁷⁵ These materials were synthesized and tested similarly, but that resulting electrochemistry differed by approximately 450 mAh/g after 100 cycles. Although these materials were discharged at different rates as indicated in **Table 2**, the FeOOH-glucose derived rods have superior cycling ability based on the reported electrochemical evaluations of the materials.

Similar Fe_3O_4 nanostructures, ovoid in shape ~500 nm long and 100-125 nm in diameter, referred to as nanospindles, were generated by Zhang et al. from previously synthesized Fe_2O_3 nanospindles. Glucose was again used as the carbon source, forming a 2-10 nm thick carbon coating. These core-shell nanospindles showed the ability to deliver over 530 mAh/g after 160 cycles with a C/5 (cycles 1-5) or C/2 (cycles 6-160) rate. The authors noted that this carbon layer also protected the integrity of the Fe_3O_4 nanospindles over multiple cycles by ex-situ TEM study after a lithiation/delithiation cycle.⁷⁶ Partially reducing hematite in an autoclave was shown to produce magnetite dendrites 2.5-6 microns long through the backbone with arms resembling a fractal structure. The intent was to design a morphology with interspaces that could better accommodate the lithiation and delithiation processes. However, this structure showed significant early capacity fade over the initial 15 cycles even in the presence of carbon coating.⁷⁷

Other approaches intended to mitigate the impacts of lattice expansion and contraction during lithiation and delithiation of Fe_3O_4 have generated composites described as “clustered” systems. A cluster refer to a group of nanoparticles that have agglomerated to form a hierarchical structure. In many cases, the cluster is a mesoscale composite containing Fe_3O_4 , carbon and/or organic polymers. A “grapelike” cluster was studied and classified by the carbon nanotube

backbone and the magnetite nanoparticles acting as “grapes” that are connected to the CNT backbone. The cluster is formed starting from an FeOOH precursor, which is coated in carbon via a glucose precursor, and then converted to magnetite. The resulting grapelike structure was confirmed by SEM and TEM imaging and showed a considerable void volume via porosimetry analysis. The grapelike structure showed improved capacity and rate capability relative to previously synthesized core-shell magnetite nanoparticles.⁷⁸ Another “urchin-like” nanocluster was synthesized by combining FeCl₃·6H₂O, pyrrole, and sodium docedyl sulfate in water to form polypyrrole coated FeOOH then calcinated to form 200-500 nm magnetite core-carbon coated spheres with 10 nm pores and an urchin-like surface. The urchin-like clusters were tested against commercially used magnetite and shown to have improved cycling capability attributed to improved capability to accommodate volume change during lithiation/delithiation.⁷⁹

Another successful morphology that accommodates volume changes during the discharge/charge process is the three dimensional hollow spheroid structure. Silk nanofibers and FeCl₃·6H₂O were dehydrated to form FeOOH/silk spheroids, then Oswald ripening progressed to form Fe₂O₃/silk hollow spheroids, when were then reduced to generate hollow, core magnetite structures with a carbon shell. The three dimensional hollow spheroid structures showed improved electrochemical performance relative to their Fe₂O₃/silk precursors, with 100% coulombic efficiency over 180 cycles and capacity exceeding 900 mAh/g.⁸⁰ Core-shell, porous spheres were also generated by a hydrothermal reaction where the carbon shell was generated by calcination of the residual ethanol from the reaction. First, porous Fe₂O₃ particles were generated then upon calcination the carbon fused the particles to form larger magnetite spheres 100-120 nm in diameter. The structure exhibited the highest capacity over 60 cycles in **Table 1**, implying a successful pathway to short Li⁺ paths lengths with high three dimensional electronic conductivity.⁸¹

Mesoporous microcuboid structures of Fe₃O₄ approximately 30 microns in length linked by a carbon matrix have been prepared, derived from FeC₂O₄·2H₂O. An advantage of this approach was the opportunity for large scale syntheses, although the method lacks the ability to provide an even carbon coating, leaving some magnetite surfaces exposed to electrolyte.⁸² Under high rate discharge at 100 mA/g, a high initial capacity of 1719 mAh/g was demonstrated, with good capacity retention of 975 mAh/g after 50 cycles.

4. Example of 2D iron oxide material which also exhibits crystallite size effects

Silver Ferrite, AgFeO₂

Layered structures or 2D materials can be useful as LIB electrodes as they allow for facile insertion and deinsertion of Li⁺ ions in two dimensions with the possibility for little structural strain during charge/discharge cycles. Silver ferrite (AgFeO₂) is a layered structure consisting of FeO₆ octahedra with Ag⁺ ions occupying the space between these layers which can exist in two distinct but similar phases: 3R, rhombohedral and 2H, hexagonal, as shown in **Figure 9**. Silver ferrite can be prepared at low temperature using a coprecipitation method.⁸³ Recently, it was demonstrated that crystallite size control of silver ferrite was achievable using the coprecipitation approach. Notably, the crystallite size control of silver ferrite was accompanied by direct formation of a silver ferrite-maghemite composite, demonstrating a new paradigm for direct synthesis of metal oxide composites.⁸⁴

The composition of the composite was affirmed by a combination of techniques, including x-ray diffraction (XRD), inductively coupled plasma-optical emission spectroscopy (ICP-OES), Raman spectroscopy, and x-ray absorption spectroscopy (XAS). A compositional range of Ag_xFeO₂ where (0.2 ≤ x ≤ 1.0) was achieved. Despite the significant change in silver concentration across the series, the lattice constants did not change and the XRD pattern only exhibited reflections corresponding to the two AgFeO₂ polymorphs where the percentage of the 3R phase increased as the silver content decreased. As the Ag/Fe ratio decreased, the crystallite size decreased, **Figure 10a**. Further characterization of these materials via Raman spectroscopy indicated the presence of maghemite (γ-Fe₂O₃) at low silver concentrations. Linear combination fitting of the Raman data showed that at a composition of Ag_{0.2}FeO₂, nearly 80% of the material is composed of maghemite, **Figure 10b**.⁸⁴ Even for high maghemite content materials, the maghemite was too amorphous to detect via XRD. The presence of maghemite in the low silver content samples was further supported by XAS, with an increase in intensity of the pre-edge for the Fe K-edge as the silver content decreased, consistent with an increase in a population of Fe³⁺ in tetrahedral interstitial sites, as are present in the maghemite structure.⁸⁴

There have been few studies regarding the application of AgFeO₂ as a cathode in lithium ion batteries. Initial studies by CV showed that Ag_{0.98}FeO₂ is electrochemically active and SEM,

EDS, and XRD data proved the formation of silver metal upon discharge.⁸³ Galvanostatic intermittent titration technique (GITT) testing indicated that as the crystallite size decreased, the polarization decreased resulting in higher voltages for the lower silver content samples. The cells were cycled at 0.15 mA/cm^2 between 1.5 and 3.5 V. The focus of these initial electrochemical evaluations was the lithium insertion process at higher voltage. As illustrated in **Figure 11**, the discharge capacity during the lithium insertion process is dependent on the Ag_xFeO_2 composition of the Ag_xFeO_2 material, and in turn, crystallite size. As the crystallite size decreases, the capacity increases. Cycled under the same conditions, maghemite ($\gamma\text{-Fe}_2\text{O}_3$) achieved a reversible capacity of 60 mAh/g, and stoichiometric AgFeO_2 with a crystallite size of $\sim 16 \text{ nm}$ achieved a reversible capacity of 62 mAh/g, while the $\text{Ag}_{0.2}\text{FeO}_2$ composite with a crystallite size of $\sim 11 \text{ nm}$ achieved a reversible capacity of 112 mAh/g after 50 cycles. The results highlight the importance of the silver ferrite-maghemite composite and crystallite size on electrochemical performance.

5. Epilogue

Material synthesis and the preparation of nanocomposites are keenly important in determining the function of materials. This review is structured largely as a case study, where the structure/function relationships among magnetite (Fe_3O_4) crystallite size, nanocomposites of Fe_3O_4 , and battery-relevant electrochemistry are delineated. Following the case study, a brief discussion of the direct synthesis and the electrochemistry of a 2D structured material, specifically, a new nanocomposite based on silver ferrite-maghemite, $\text{AgFeO}_2\text{-}\gamma\text{Fe}_2\text{O}_3$, is included. The case study illustrates through a review of the literature how structure/function relationships impacting battery relevant electrochemistry continue to evolve, while the shorter discussions of less studied $\text{AgFeO}_2\text{-}\gamma\text{Fe}_2\text{O}_3$ illustrate the growing need for future exploration of structure/function relationships involving battery-relevant electrochemistry through synthetic control of new electroactive materials and composites. As new battery materials and new strategies for battery technologies evolve, the critical role of crystallite size on battery electrochemistry will likely continue as a paradigm for the next generation of batteries.

Acknowledgement

The preparation of this manuscript was supported as part of the Center for Mesoscale Transport Properties, an Energy Frontier Research Center supported by the U.S. Department of Energy, Office of Science, Basic Energy Sciences, under award #DE-SC0012673. C.N.G. acknowledges support from the National Science Foundation funded Research Experience for Undergraduates Site: Nanotechnology for Health, Energy and the Environment at Stony Brook University. Any opinions, findings, and conclusions or recommendations expressed in this material are those of the authors and do not necessarily reflect the views of the National Science Foundation.

List of Figures.

Figure 1. The number of papers published regarding nanotechnology, lithium ion batteries (LIBs), nanotechnologies integration into LIBs, and magnetite's incorporation into LIBs.

*Values for 2015 were taken in June 2015 and projected to be consistent throughout the remainder of the year.

Figure 2. Crystal structure of magnetite (Fe_3O_4).

Figure 3. Discharge profiles of lithium cells containing magnetite (Fe_3O_4) of varying crystallite size prepared by coprecipitation technique.

Figure 4. Comparison of x-ray absorption near edge structure (XANES) spectra for 26, 10, and 8 nm magnetite (Fe_3O_4).

Figure 5. Electrodes prepared with (i) 28 and (ii) 8 nm magnetite (Fe_3O_4) **a)** Aggregate size distributions in undischarged electrodes. Inset: Bright-field transmission electron microscopy (TEM) images of sectioned electrodes fabricated with 8 and 28 nm sized Fe_3O_4 . **b)** Transmission x-ray microscopy - x-ray absorption near edge structure (TXM-XANES) images of electrodes discharged to 100 mAh/g. Selected regions A and B are magnified in each image.

Figure 6. Conceptual models of magnetite (Fe_3O_4) nanoparticle – carbon heterostructures. **a)** Graphene sheet transformed to a graphene oxide composite by Hummers method. The hydroxyl, oxide, and carboxylic acid substituents provide nucleation sites for magnetite bind to the sheet. **b)** Carbon source converted to an evenly dispersed carbon coating on the Fe_3O_4 surface – referred to as core shell particles.

Figure 7. Structure of silver ferrite (AgFeO_2). **a)** Rhombohedral (3R). **b)** Hexagonal (2H).

Figure 8. Characterization data for silver ferrite-maghemite (AgFeO_2 - γ - Fe_2O_3) composites **a)** Dependence of crystallite size on silver concentration, **b)** Percent AgFeO_2 determined by linear combination fit (LCF) of Raman data versus measured Ag/Fe ratio. **c)** Discharge capacity versus cycle number for lithium cells containing silver ferrite-maghemite (AgFeO_2 - γ - Fe_2O_3) composite electrodes.

Table 1: Electrochemical performance of magnetite (Fe_3O_4) with different morphologies.

Fe_3O_4 Morphology	Size (nm)	Fe_3O_4 in electrode	Initial Capacity, Rate, Voltage Limit	Capacity, Rate, # Cycles	Ref.
hollow spheres	30-40	70%	1261 mAh/g, 0.1C, 0.01 – 3.0 V	852 mAh/g, 1C, cycles 5 – 50	⁴⁶
hexahedra	length, 200	80%	1304 mAh/g, 100 mA/g, 0.01 – 3.0 V	644.1 mAh/g, 100 mA/g, 40	⁴⁹
octahedra	length, 1000 - 3000	80%	1216 mA/g, 100 mA/g, 0.01 – 3.0 V	350.5 mAh/g, 100 mA/g, 40	⁴⁹
polyhedra	120-150	50%	2632 mAh/g, 50 mA/g, 0.05 – 3.0 V	1100 mAh/g, 50 mA/g, 50	⁴⁸
nanowires	50	60%	2416 mAh/g, 50 mA/g, 0.01 – 3.0 V	774 mAh/g, 50 mA/g, 50	⁸⁵
nanowires	20-50	70%	1240 mAh/g, C/10, ~0.1 – 3.0 V	820 mAh/g, C/10, 50	⁸⁶
submicron spheres composed of nanospheres	30	40%	1332 mAh/g, 0.2 C, 0.01 – 3.0 V	1100 mAh/g, 0.2 C, 60	⁵⁷
hollow spheres organized by nanosheets	10	70%	1614 mAh/g, 500 mA/g, 0.01 – 3.0 V	1046 mAh/g, 500 mA/g, 100	⁴⁵
hollow microspheres	4180	70%	945 mAh/g, 0.1C, 0.02 – 3.0 V	830 mAh/g, 0.1 C, 35	⁴⁷
pyramid	10	100%	1800 mAh/g, 40 mA/g, 0.05 – 3.0 V	1300 mAh/g, 40 mA/g, 7	⁸⁷

Table 2. Delivered capacities for selected magnetite (Fe_3O_4) electrode heterostructures. The active material composition and morphology, Fe_3O_4 crystallite size, electrode formulation, carbon type, initial capacity, and final capacity are provided, with the relevant rate, voltage limits and reported cycle number.

Active material composition and morphology	Fe_3O_4 crystallite size	Fe_3O_4 in active material	Active material	Carbon additive	Initial Capacity, Rate, Voltage limit	Final capacity, cycle number	Ref.
Fe_3O_4 @C core-shell nanotubes	250 nm	93%	80%	10%, SP	1213 mAh/g, 100 mA/g, 0.01 – 3.0 V; 500 mA/g, 0.01 – 3.0 V	808 mAh/g, 20 cycles; 560 mAh/g 100 cycles	⁷³
Fe_3O_4 @C core – shell nanorods	200 nm	96%	80%	10%, SP	2117 mAh/g, 1C, 0.01 – 3.0 V	807 mAh/g, 100 cycles	⁷⁴
Fe_3O_4 @C core – shell nanorods	150-200 nm	NR	75%	15%, AB	1126 mAh/g, 0.1C, 0.01 – 3.0 V	394 mAh/g, 100 cycles	⁷⁵
“grapecluster”: core – shell Fe_3O_4 @C nanoparticles on CNT	150 nm	91%	65%	20%, SP	1450 (w/CNT) 900 (w/o CNT) mAh/g, 60 mA/g, 0.01 – 3.0 V	693 mAh/g, 200 cycles	⁷⁸
Fe_3O_4 nanorods embedded in SWCNT	not reported	not reported	not reported	not reported	1000 mAh/g 0.1C cycles 1-5, 1C cycles 6-50, 0.005 – 3.0 V; 1030 mAh/g 0.1C cycles 1-5, 5C cycles 6-100, 0.005 – 3.0 V	1050 mAh/g 50 cycles 690 mAh/g 100 cycles	⁸⁸
porous core – shell Fe_3O_4 @C nanospheres	100-120 nm	70%	75%	15%, Ketjen black	1691 mAh/g, 100 mA/g, 0.01 – 3.0 V	1100 mAh/g, 60 cycles	⁸¹
core – shell N-doped Fe_3O_4 @C nanoparticles	100 nm	84%	70%	15%, CB	1173 mAh/g, 500 mA/g, 0.01 – 3.0 V	976 mAh/g, 50 cycles	⁷¹
core –shell Fe_3O_4 @C hollow spheroids	90-30nm	very high	65%	25%, SP	1369 mAh/g, 200 mA/g 0.05 – 3.0 V	900 mAh/g, 180 cycles	⁸⁰
hollow Fe_3O_4 microspheres	44-79 nm	100%	70%	20%, AB, CNTs 1:1	1200 mAh/g, 60 mA/g, 0.01-3.0 V	900 mAh/g, 30 cycles	⁵¹
onion – like carbon coated Fe_3O_4	30-60 nm	NR	80%	10%, CB	1449 mAh/g, 100 mA/g,	918 mAh/g, 300 cycles	⁶⁸

nanoparticles					0.01 – 3.0 V		
carbon coated Fe ₃ O ₄ nanospindles	30 nm	79%	70%	15%, CB	749 mAh/g, 0.2C cycle 1-5, 0.5C cycle 6-160, ~0.01 – 3 V	530 mAh/g, 160 cycles	76
carbon encapsulated Fe ₃ O ₄	18.2 nm	68.7%	80%	10%, CB	1499 mAh/g, 1000 mA/g, 0.005 – 3.0 V	980 mAh/g, 350 cycles	89
carbon coated Fe ₃ O ₄ dendrites	20 nm	very high	80%	10%, CB	1100 mAh/g, C/10, 0 – 3.0 V	405 mAh/g, 50 cycles	77
carbon coated Fe ₃ O ₄ microcuboids	20 nm	98%	70%	20%, AB	1719 mAh/g, 100 mA/g, 0.05 – 3.0 V	975 mAh/g, 50 cycles	82
carbon coated Fe ₃ O ₄ nanoparticles on CNTs	10-15 nm	90%	80%	10% C	1030 mAh/g, 50 mA/g, 0.5 – 2.5 V	620 mAh/g, 50 cycles	72
core – shell Fe ₃ O ₄ @C nanoparticles	12 nm	NR	70%	15%, SP	1310 mAh/g, 100 mA/g, 0.1 – 3.0 V	859 mAh/g, 50 cycles	70
carbon coated sea urchin – like Fe ₃ O ₄ nanoclusters	10.8 nm	88%	70%	15%, SP	1228 mAh/g, 100 mA/g, 0.01 – 3.0 V	900 mAh/g, 10 cycles	79
core – shell Fe ₃ O ₄ @C nanoparticles	10 nm	93%	70%	15%, SP	1400 mAh/g, 185 mA/g, 0.01 – 3.0 V	700 mAh/g, 400 cycles	69
rGO/Fe ₃ O ₄ paper	NR	65%	85%	10%, SP-CB	1100 mAh/g, 1C, 0.01 – 3.0 V	1140 mAh/g, 220 cycles	52
Fe ₃ O ₄ /G nanoscrolls	NR	50%	90%	0%	1720 mAh/g, 0.1C, 0.01 – 3.0 V	1010 mAh/g, 50 cycles	59
C coated flower-like Fe ₃ O ₄ / G microstructure	NR	NR	80%	10%, AB	1602 mAh/g, 0.2C, 0.01 – 3.0 V	1439 mAh/g, 47 cycles	60
semi exfoliated reduced graphite oxide, Fe ₃ O ₄ /graphite oxide nanosheets	NR	NR	100%	0%	1616 mAh/g, 75 mA/g, 0.01 – 3.0 V	1309 mAh/g, 10 cycles	58
Fe ₃ O ₄ nanocrystals on C matrix	70 nm	NR	100%	0%	863 mAh/g, 0.1C, 0.1 – 3.0 V	777 mAh/g, 30 cycles	66
Fe ₃ O ₄ /G nanosheets	20-70 nm	NR	80%	10%, CB	1320 mAh/g, 5C, 0.01 – 3.0V	650 mAh/g, 30 cycles	57
Fe ₃ O ₄ /G nanosheets	30-50 nm	70%	80%	10%, AB	1040 mAh/g, 1000 mA/g 0.01 – 3.0 V	335 mAh/g, 300 cycles	54
Fe ₃ O ₄ /G nanosheets	40 nm	NR	80%	10%, AB	1334 mAh/g 928 mA/g,	504 mAh/g, 50 cycles	55

					0.01 – 3.0 V		
Fe ₃ O ₄ on C foam – like composite	13-27 nm	55%	80%	10%, super C65	1710 mAh/g, 100 mA/g, Cyc. 3-150 500 mA/g, 0.01 – 3.0 V	950 mAh/g, 150 cycles	64
Fe ₃ O ₄ /G nanosheets	20 nm	11%	80%	10%, AB	1976 mAh/g, 200 mA/g, 0.001 – 3.0 V	1243 mAh/g, 50 cycles	53
Fe ₃ O ₄ /G nanosheets	10-20 nm	55%	80%	10%, SP-Li	1126 mAh/g, 0.1C, 0.01 – 3.0 V	500 mAh/g, 100 cycles	61
Fe ₃ O ₄ -G nanocomposite	not reported	78%	75%	15%, SP	1060 mAh/g, 100 mA/g, 0.1 – 3.0 V	1048 mAh/g, 85 cycles	90
Fe ₃ O ₄ /G composites	15 nm	40%	85%	10%, AB	1545 mAh/g, 0.05C, 0.001 – 3.0 V	675 mAh/g, 50 cycles	62
Fe ₃ O ₄ @G- foam nanosheet	7-15 nm	NR	100%	0%	1671 mAh/g, 1C, 0.01 – 3.0 V	1200 mAh/g, 500 cycles	63
Fe ₃ O ₄ /G nanosheet	10 nm	42%	82%	8%, SP, KS-6 1:1	700 mAh/g, 0.2C, 0.01 – 3.0 V;	575 mAh/g, 50 cycles	56
G wrapped Fe ₃ O ₄	not reported	87%	80%	10%, SP	1400 mAh/g, 35 mA/g 0.001 – 3.0 V	770 mAh/g, 100 cycles	91
G encapsulated Fe ₃ O ₄	12 nm	62%	80%	10%, AB	1080 mAh/g, 100 mA/g, 0 – 3.0 V	650 mAh/g, 100 cycles	92
Fe ₃ O ₄ on C foamlike composite	15-20 nm	46%	80%	10%, SP-CB	1263 mAh/g, 200 mA/g, 0.005 – 3.0 V	1008 mAh/g, 400 cycles	65
Fe ₃ O ₄ on CNTs	5 nm	41%	80%	10%, AB	840 mAh/g, 0.1C, 0.02 – 3.0 V	390 mAh/g, 75 cycles	67
Fe ₃ O ₄ -CNT composite	very small	66.7%	90%	0%	988 mAh/g, 100 mA/g, 0.02 – 3.0 V	650 mAh/g, 145 cycles	93
CNT-Fe ₃ O ₄ coaxial nanocables	9.5 nm	not reported	80%	10% AB	1431 mAh/g, 200 mA/g, 0.01 – 3.0 V	1290 mAh/g, 200 mA/g, 80 cycles	94
					800 mAh/g, 2000 mA/g, 0.01 – 3.0 V	690 mAh/g, 2000 mA/g, 200 cycles	
CNT-reduced GO Fe ₃ O ₄ nanocomposite	7 nm	53%	80%	10%, SP	1277 mAh/g, 200 mA/g, 0.00 – 3.0 V	680 mAh/g, 100 cycles	95
Fe ₃ O ₄ sheath on aligned CNT	5-7 nm	50-60%	N/A	N/A	1814 mAh/g, 100 mA/g, 0.1 – 3.0 V	1670 mAh/g, 100 cycles	96

AB = acetylene black, C = carbon, CB = carbon black, G = graphene, GO = graphene oxide, SP = Super-P carbon black, CNT = carbon nanotubes, SWCNT = single walled carbon nanotubes

References

1. J. B. Goodenough and K.-S. Park, *J Am Chem Soc*, 2013, **135**, 1167-1176.
2. A. Yoshino, *Angewandte Chemie-International Edition*, 2012, **51**, 5798-5800.
3. H. Kumar, S. Rajan and A. K. Shukla, *Science progress*, 2012, **95**, 283-314.
4. S. Flandrois and B. Simon, *Carbon*, 1999, **37**, 165-180.
5. L. W. Ji, Z. Lin, M. Alcoutlabi and X. W. Zhang, *Energy & Environmental Science*, 2011, **4**, 2682-2699.
6. M. S. Whittingham, *Chemical Reviews*, 2004, **104**, 4271-4302.
7. J. W. Fergus, *Journal of Power Sources*, 2010, **195**, 939-954.
8. M. M. Huie, R. A. DiLeo, A. C. Marschilok, K. J. Takeuchi and E. S. Takeuchi, *ACS Appl. Mater. Interfaces*, 2015, **7**, 11724-11731.
9. R. A. Di Leo, A. C. Marschilok, K. J. Takeuchi and E. S. Takeuchi, *Electrochim. Acta*, 2013, **109**, 27-32.
10. R. A. DiLeo, A. C. Marschilok, K. J. Takeuchi and E. S. Takeuchi, *J. Electrochem. Soc.*, 2013, **160**, A1399-A1405.
11. Y. J. Kim, A. C. Marschilok, K. J. Takeuchi and E. S. Takeuchi, *J. Power Sources*, 2011, **196**, 6781-6787.
12. D. C. Bock, A. C. Marschilok, K. J. Takeuchi and E. S. Takeuchi, *J. Power Sources*, 2013, **231**, 219-225.
13. D. C. Bock, K. J. Takeuchi, A. C. Marschilok and E. S. Takeuchi, *Dalton Trans.*, 2013, **42**, 13981-13989.
14. D. C. Bock, K. J. Takeuchi, A. C. Marschilok and E. S. Takeuchi, *Phys. Chem. Chem. Phys.*, 2015, **17**, 2034-2042.
15. D. C. Bock, R. V. Tappero, K. J. Takeuchi, A. C. Marschilok and E. S. Takeuchi, *ACS Appl. Mater. Interfaces*, 2015, **7**, 5429-5437.
16. K. Mizushima, P. C. Jones, P. J. Wiseman and J. B. Goodenough, *Materials Research Bulletin*, 1980, **15**, 783-789.
17. A. Rougier, I. Saadoun, P. Gravereau, P. Willmann and C. Delmas, *Solid State Ionics*, 1996, **90**, 83-90.
18. S. M. Dou, *Journal of Solid State Electrochemistry*, 2013, **17**, 911-926.

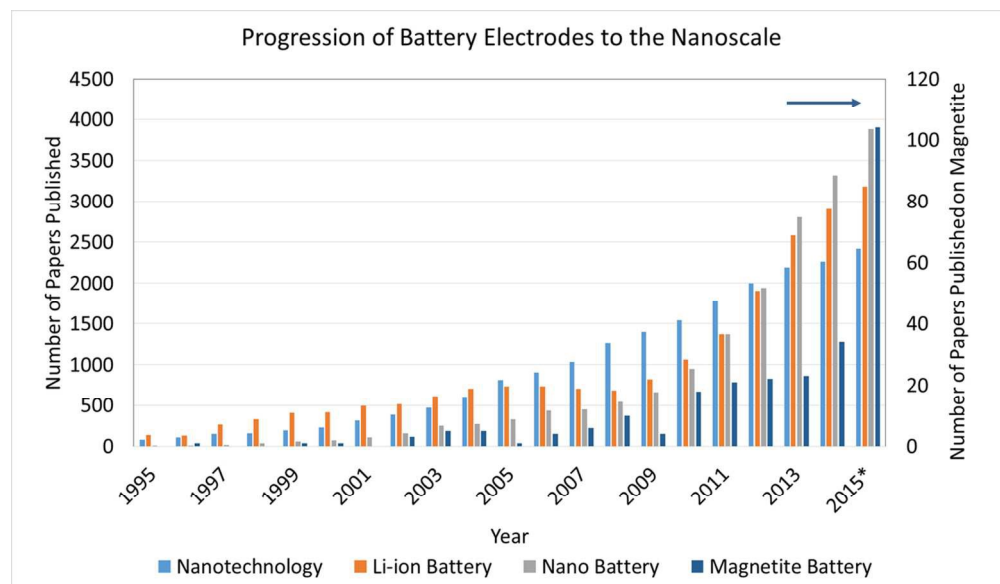
19. B. Xu, D. Qian, Z. Wang and Y. S. Meng, *Materials Science and Engineering: R: Reports*, 2012, **73**, 51-65.
20. S.-T. Myung, K. Amine and Y.-K. Sun, *Journal of Power Sources*, 2015, **283**, 219-236.
21. R. Malini, U. Uma, T. Sheela, M. Ganesan and N. G. Renganathan, *Ionics*, 2009, **15**, 301-307.
22. L. W. Su, Y. Jing and Z. Zhou, *Nanoscale*, 2011, **3**, 3967-3983.
23. X. R. Wang and G. Yushin, *Energy & Environmental Science*, 2015, **8**, 1889-1904.
24. Z. S. Wu, G. M. Zhou, L. C. Yin, W. Ren, F. Li and H. M. Cheng, *Nano Energy*, 2012, **1**, 107-131.
25. U. Kasavajjula, C. S. Wang and A. J. Appleby, *Journal of Power Sources*, 2007, **163**, 1003-1039.
26. M. C. Menard, K. J. Takeuchi, A. C. Marschilok and E. S. Takeuchi, *Phys. Chem. Chem. Phys.*, 2013, **15**, 18539-18548.
27. W. D. Nesse, *Introduction to Mineralogy*, Oxford University Press Inc., Oxford, Second edn., 2012.
28. V. Sivakumar, S. Kumar, C. A. Ross and Y. Shao-Horn, *IEEE Trans. Magn.*, 2007, **43**, 3121-3123.
29. J. B. Goodenough, *Accounts of chemical research*, 2012, **46**, 1053-1061.
30. T. Yamada, K. Morita, K. Kume, H. Yoshikawa and K. Awaga, *J. Mater. Chem. C*, 2014, **2**, 5183-5188.
31. K. W. Knehr, N. W. Brady, C. A. Cama, D. C. Bock, Z. Lin, C. N. Lininger, A. C. Marschilok, K. J. Takeuchi, E. S. Takeuchi and A. C. West, *Journal of the Electrochemical Society*, 2015, **162**, A2817-A2826.
32. K. W. Knehr, N. W. Brady, C. N. Lininger, C. A. Cama, D. C. Bock, Z. Lin, A. C. Marschilok, K. J. Takeuchi, E. S. Takeuchi and A. C. West, *ECS Transactions*, 2015, **69**, 7-19.
33. S. Komaba, T. Mikumo and A. Ogata, *Electrochem. Commun.*, 2008, **10**, 1276-1279.
34. S. Komaba, T. Mikumo, N. Yabuuchi, A. Ogata, H. Yoshida and Y. Yamada, *J. Electrochem. Soc.*, 2010, **157**, A60-A65.
35. S. Zhu, A. C. Marschilok, E. S. Takeuchi and K. J. Takeuchi, *Electrochem. Solid-State Lett.*, 2009, **12**, A91-A94.

36. S. Zhu, A. C. Marschilok, E. S. Takeuchi, G. T. Yee, G. Wang and K. J. Takeuchi, *J. Electrochem. Soc.*, 2010, **157**, A1158-A1163.
37. M. C. Menard, A. C. Marschilok, K. J. Takeuchi and E. S. Takeuchi, *Electrochim. Acta*, 2013, **94**, 320-326.
38. D. C. Bock, A. C. Marschilok, K. J. Takeuchi, E. S. Takeuchi, K. C. Kirshenbaum, J. Wang, W. Zhang, F. Wang, J. Wang, E. S. Takeuchi, A. C. Marschilok, K. J. Takeuchi and E. S. Takeuchi, *ACS Appl Mater Interfaces*, 2015, **7**, 13457-13466.
39. C. W. Kwon, M. Quintin, S. Mornet, C. Barbieri, O. Devos, G. Campet and M. H. Delville, *J. Electrochem. Soc.*, 2004, **151**, A1445-A1449.
40. G. F. Goya, T. S. Berquo, F. C. Fonseca and M. P. Morales, *Journal of Applied Physics*, 2003, **94**, 3520-3528.
41. A. G. Roca, J. F. Marco, M. d. P. Morales and C. J. Serna, *J. Phys. Chem. C*, 2007, **111**, 18577-18584.
42. J. Santoyo Salazar, L. Perez, O. de Abril, L. Truong Phuoc, D. Ihiwakrim, M. Vazquez, J.-M. Greneche, S. Begin-Colin and G. Pourroy, *Chem. Mater.*, 2011, **23**, 1379-1386.
43. S. J. Iyengar, M. Joy, C. K. Ghosh, S. Dey, R. K. Kotnala and S. Ghosh, *RSC Adv.*, 2014, **4**, 64919-64929.
44. C. Piquer, M. A. Laguna-Marco, A. G. Roca, R. Boada, C. Guglieri and J. Chaboy, *Journal of Physical Chemistry C*, 2014, **118**, 1332-1346.
45. F.-X. Ma, H. Hu, H. B. Wu, C.-Y. Xu, Z. Xu, L. Zhen and X. W. Lou, *Adv. Mater. (Weinheim, Ger.)*, 2015, DOI: 10.1002/adma.201501130, Ahead of Print.
46. Q. Q. Xiong, J. P. Tu, Y. Lu, J. Chen, Y. X. Yu, Y. Q. Qiao, X. L. Wang and C. D. Gu, *J. Phys. Chem. C*, 2012, **116**, 6495-6502.
47. H.-S. Lim, B.-Y. Jung, Y.-K. Sun and K.-D. Suh, *Electrochim. Acta*, 2012, **75**, 123-130.
48. D. Su, J. Horvat, P. Munroe, H. Ahn, A. R. Ranjbartoreh and G. Wang, *Chem. - Eur. J.*, 2012, **18**, 488-497, S488/481-S488/483.
49. Q. Wang, D. Chen, J. Chen, C. Lai, L. Li and C. Wang, *Mater. Lett.*, 2015, **141**, 319-322.
50. A. S. Fialkov, *Russ. J. Electrochem.*, 2000, **36**, 345-366.
51. Y. Deng, Q. Zhang, Z. Shi, L. Han, F. Peng and G. Chen, *Electrochim. Acta*, 2012, **76**, 495-503.
52. K. Zhang, W. Zhao, J.-T. Lee, G. Jang, X. Shi and J. H. Park, *J. Mater. Chem. A*, 2014, **2**, 9636-9644.

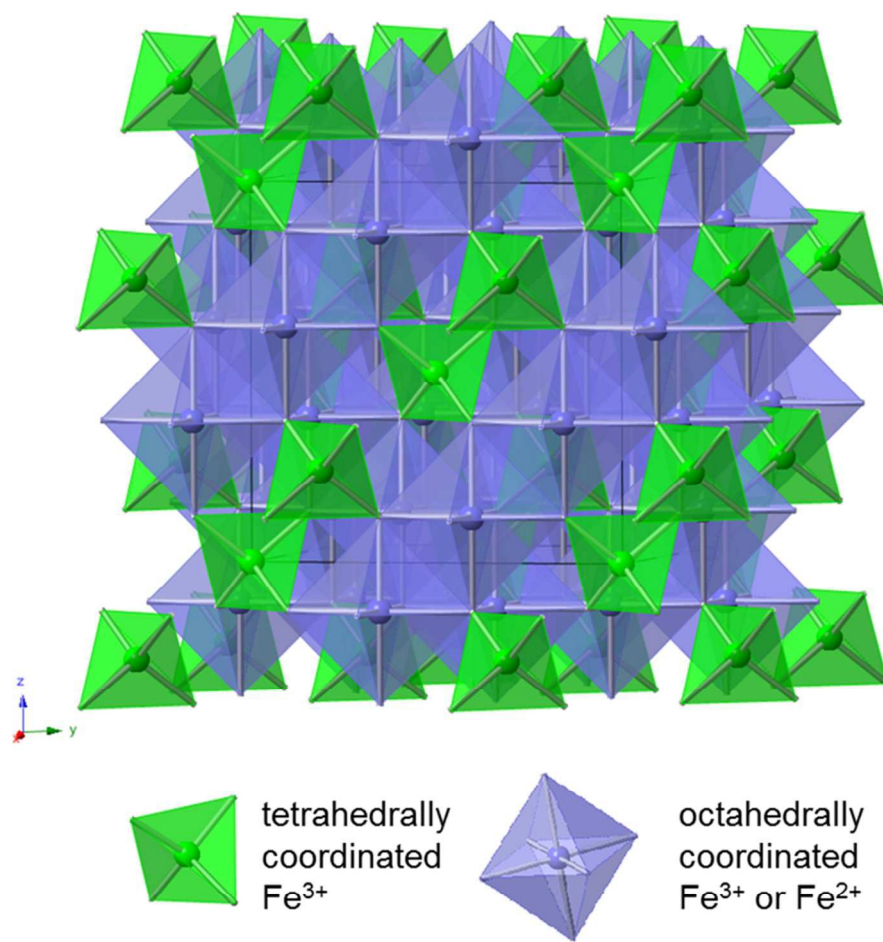
53. J. Zai, C. Yu, Q. Zou, L. Tao, K. Wang, Q. Han, B. Li, Y. Xiao, X. Qian and R. Qi, *RSC Adv.*, 2012, **2**, 4397-4403.
54. J. Zhou, H. Song, L. Ma and X. Chen, *RSC Adv.*, 2011, **1**, 782-791.
55. A. Hu, X. Chen, Y. Tang, L. Yang, H. Xiao and B. Fan, *Mater. Lett.*, 2013, **91**, 315-318.
56. C.-T. Hsieh, J.-Y. Lin and C.-Y. Mo, *Electrochim. Acta*, 2011, **58**, 119-124.
57. S. Wang, J. Zhang and C. Chen, *J. Power Sources*, 2010, **195**, 5379-5381.
58. R. Ravikumar and S. Gopukumar, *J. Power Sources*, 2015, **289**, 146-153.
59. J. Zhao, B. Yang, Z. Zheng, J. Yang, Z. Yang, P. Zhang, W. Ren and X. Yan, *ACS Appl. Mater. Interfaces*, 2014, **6**, 9890-9896.
60. Q. Guo, X. Guo, K. Du, H. Ge and F. Wang, *Int. J. Hydrogen Energy*, 2015, **40**, 1846-1851.
61. T. Yoon, J. Kim, J. Kim and J. K. Lee, *Energies (Basel, Switz.)*, 2013, **6**, 4830-4840.
62. M. Sathish, T. Tomai and I. Honma, *J. Power Sources*, 2012, **217**, 85-91.
63. X. Hu, M. Ma, M. Zeng, Y. Sun, L. Chen, Y. Xue, T. Zhang, X. Ai, R. G. Mendes, M. H. Rummeli and L. Fu, *ACS Appl. Mater. Interfaces*, 2014, **6**, 22527-22533.
64. E. Kang, Y. S. Jung, A. S. Cavanagh, G.-H. Kim, S. M. George, A. C. Dillon, J. K. Kim and J. Lee, *Adv. Funct. Mater.*, 2011, **21**, 2430-2438.
65. F. Wu, R. Huang, D. Mu, B. Wu and S. Chen, *ACS Appl Mater Interfaces*, 2014, **6**, 19254-19264.
66. Y. Piao, H. S. Kim, Y.-E. Sung and T. Hyeon, *Chem. Commun. (Cambridge, U. K.)*, 2010, **46**, 118-120.
67. J. P. Cheng, J. Yu, D. Shi, D. S. Wang, Y. F. Liu, F. Liu, X. B. Zhang and J. G. Li, *Appl. Phys. A: Mater. Sci. Process.*, 2012, **106**, 837-842.
68. N. Bi, X. Liu, N. Wu, C. Cui and Y. Sun, *RSC Adv.*, 2015, **5**, 32452-32459.
69. S.-D. Seo, D.-H. Lee, H.-W. Shim, S. Lee and D.-W. Kim, *J. Am. Ceram. Soc.*, 2014, **97**, 1413-1420.
70. H. S. Kim, S. G. Kwon, S. H. Kang, Y. Piao and Y.-E. Sung, *Electrochim. Acta*, 2014, **136**, 47-51.
71. C. Lei, F. Han, D. Li, W.-C. Li, Q. Sun, X.-Q. Zhang and A.-H. Lu, *Nanoscale*, 2013, **5**, 1168-1175.

72. D.-Y. Park and S.-T. Myung, *ACS Appl. Mater. Interfaces*, 2014, **6**, 11749-11757.
73. H. Xia, Y. Wan, G. Yuan, Y. Fu and X. Wang, *J. Power Sources*, 2013, **241**, 486-493.
74. T. Zhu, J. S. Chen and X. W. Lou, *J. Phys. Chem. C*, 2011, **115**, 9814-9820.
75. H. Liu, G. Wang, J. Wang and D. Wexler, *Electrochem. Commun.*, 2008, **10**, 1879-1882.
76. W.-M. Zhang, X.-L. Wu, J.-S. Hu, Y.-G. Guo and L.-J. Wan, *Adv. Funct. Mater.*, 2008, **18**, 3941-3946.
77. M. Zhang, X. Yin, Z. Du, S. Liu, L. Chen, Q. Li, H. Jin, K. Peng and T. Wang, *Solid State Sci.*, 2010, **12**, 2024-2029.
78. J. Liu, J. Ni, Y. Zhao, H. Wang and L. Gao, *J. Mater. Chem. A*, 2013, **1**, 12879-12884.
79. J. E. Lee, S.-H. Yu, D. J. Lee, D.-C. Lee, S. I. Han, Y.-E. Sung and T. Hyeon, *Energy Environ. Sci.*, 2012, **5**, 9528-9533.
80. W. Sheng, G. Zhu, D. L. Kaplan, C. Cao, H. Zhu and Q. Lu, *Nanotechnology*, 2015, **26**, 115603/115601-115603/115607.
81. Y. Luo, X. Zhou, Y. Zhong, M. Yang, J. Wei and Z. Zhou, *Electrochim. Acta*, 2015, **154**, 136-141.
82. M. Li, W. Wang, M. Yang, F. Lv, L. Cao, Y. Tang, R. Sun and Z. Lu, *RSC Adv.*, 2015, **5**, 7356-7362.
83. K. E. Farley, A. C. Marschilok, E. S. Takeuchi and K. J. Takeuchi, *Electrochem Solid St*, 2012, **15**, A23-A27.
84. J. L. Durham, K. Kirshenbaum, E. S. Takeuchi, A. C. Marschilok and K. J. Takeuchi, *Chemical Communications*, 2015, **51**, 5120-5123.
85. D. Su, H.-J. Ahn and G. Wang, *J. Power Sources*, 2013, **244**, 742-746.
86. T. Muraliganth, A. V. Murugan and A. Manthiram, *Chemical Communications*, 2009, DOI: 10.1039/b916376j, 7360-7362.
87. E. S. Takeuchi, A. C. Marschilok, K. J. Takeuchi, A. Ignatov, Z. Zhong and M. Croft, *Energy Environ. Sci.*, 2013, **6**, 1465-1463.
88. C. Ban, Z. Wu, D. T. Gillaspie, L. Chen, Y. Yan, J. L. Blackburn and A. C. Dillon, *Advanced Energy Materials*, 2010, **22**, E145-E149.
89. C. He, S. Wu, N. Zhao, C. Shi, E. Liu and J. Li, *ACS Nano*, 2013, **7**, 4459-4469.
90. P. C. Lian, X. F. Zhu, H. F. Xiang, Z. Li, W. S. Yang and H. H. Wang, *Electrochimica Acta*, 2010, **56**, 834-840.

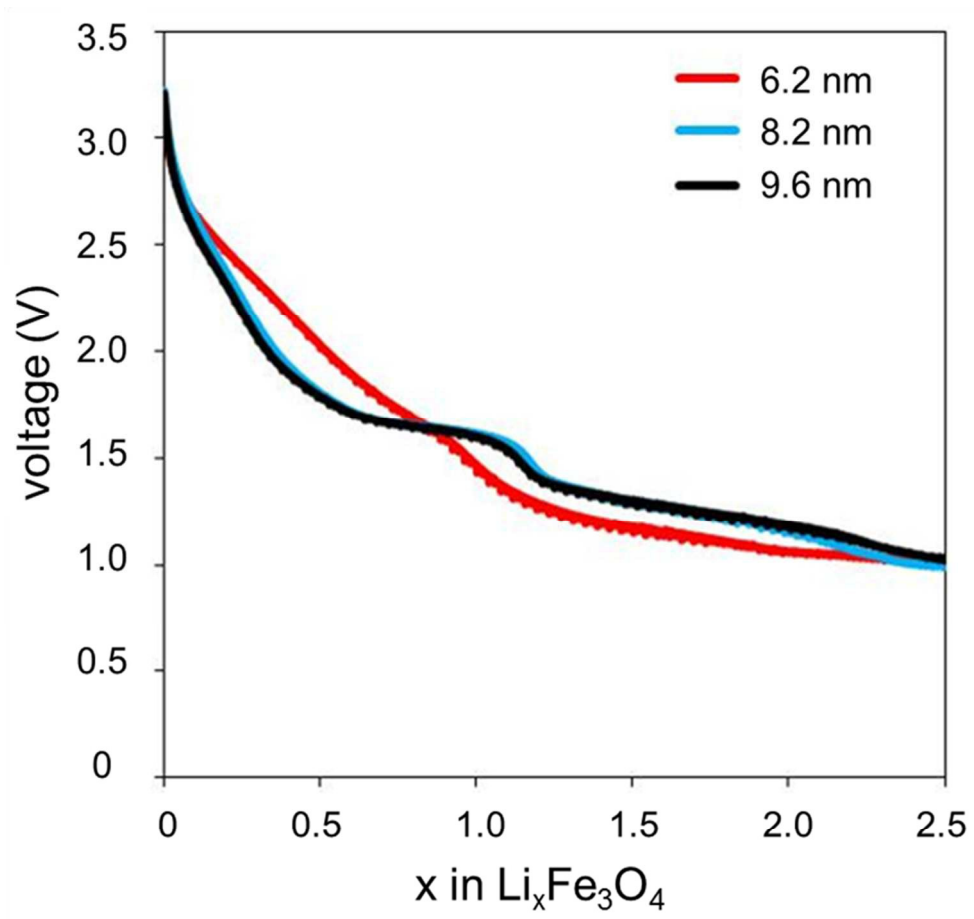
91. G. M. Zhou, D. W. Wang, F. Li, L. L. Zhang, N. Li, Z. S. Wu, L. Wen, G. Q. Lu and H. M. Cheng, *Chemistry of Materials*, 2010, **22**, 5306-5313.
92. J. Z. Wang, C. Zhong, D. Wexler, N. H. Idris, Z. X. Wang, L. Q. Chen and H. K. Liu, *Chemistry-a European Journal*, 2011, **17**, 661-667.
93. Y. He, L. Huang, J. S. Cai, X. M. Zheng and S. G. Sun, *Electrochimica Acta*, 2010, **55**, 1140-1144.
94. J. Cheng, B. Wang, C.-M. Park, Y. Wu, H. Huang and F. Nie, *Chemistry – A European Journal*, 2013, **19**, 9866-9874.
95. S. Yang, C. Cao, G. Li, Y. Sun, P. Huang, F. Wei and W. Song, *Nano Research*, 2015, **8**, 1339-1347.
96. Y. Wu, Y. Wei, J. Wang, K. Jiang and S. Fan, *Nano Letters*, 2013, **13**, 818-823.



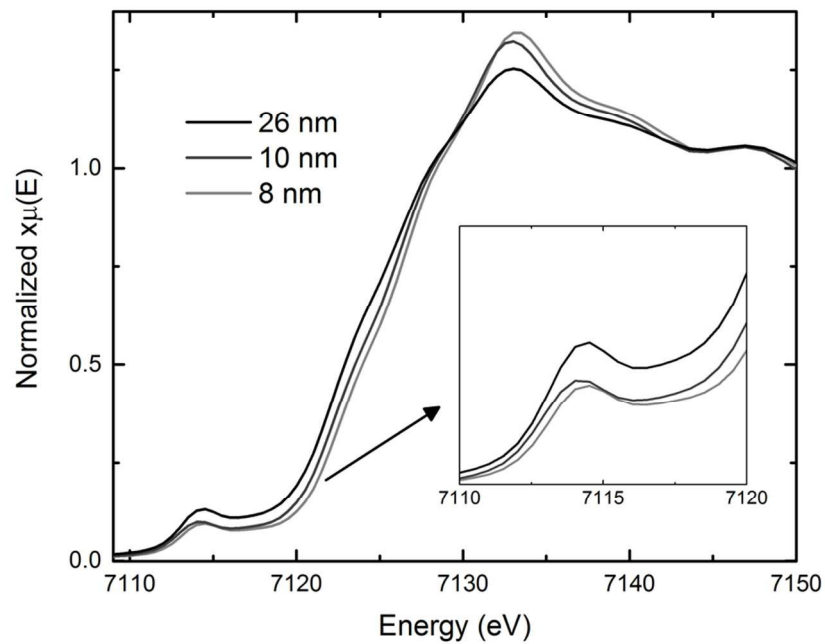
474x275mm (72 x 72 DPI)



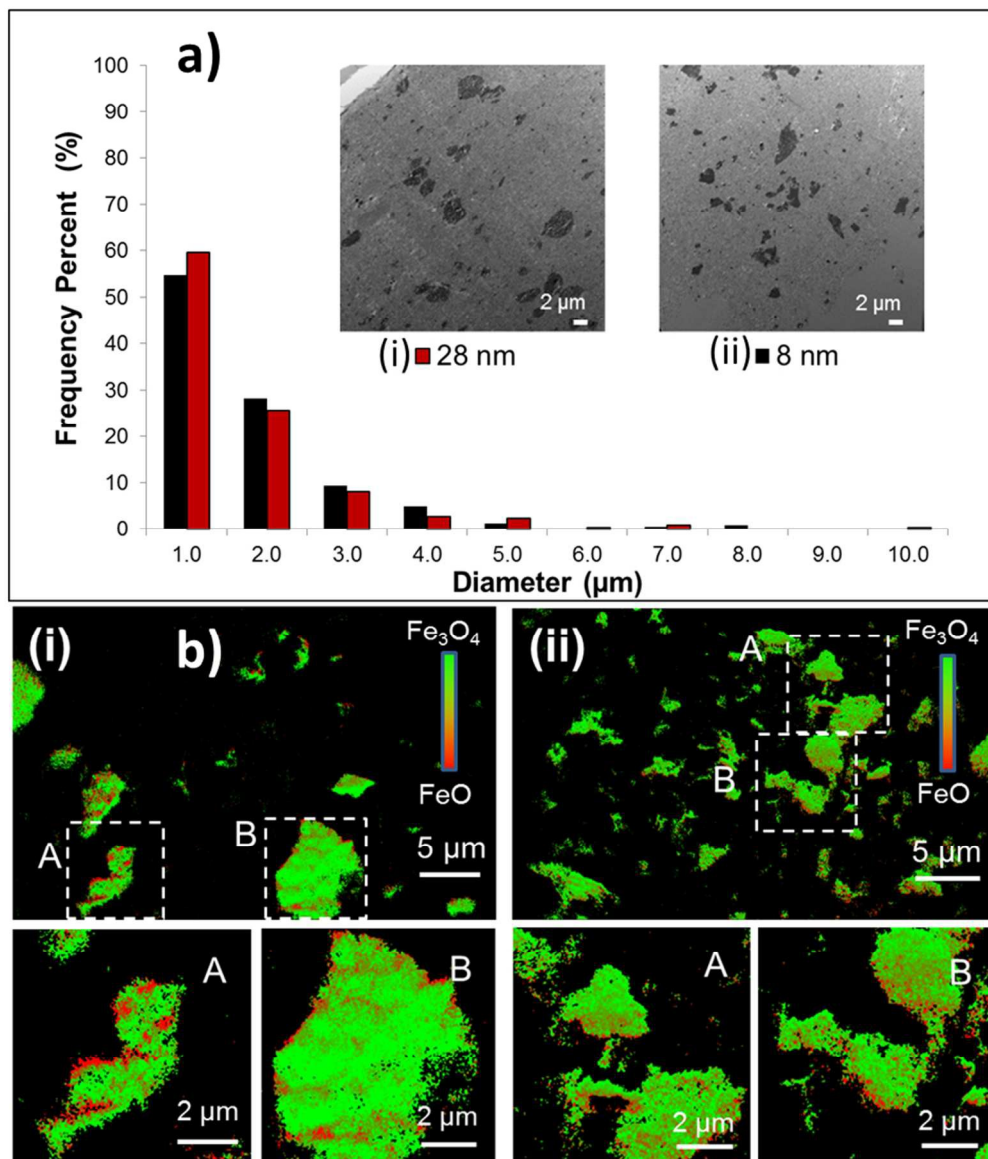
327x335mm (72 x 72 DPI)



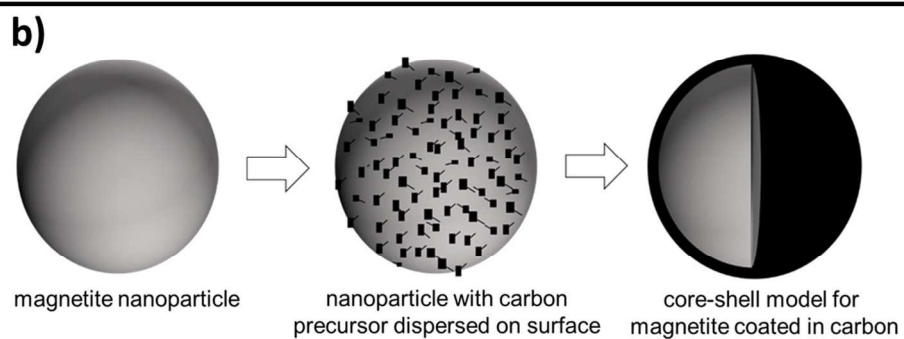
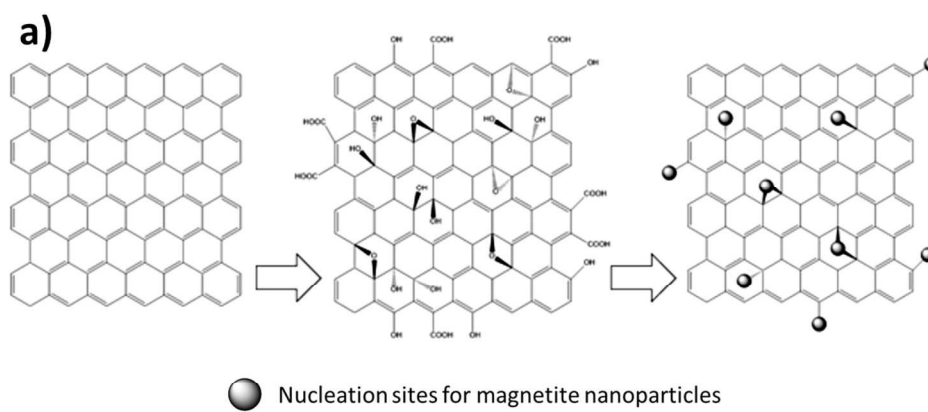
339x312mm (72 x 72 DPI)



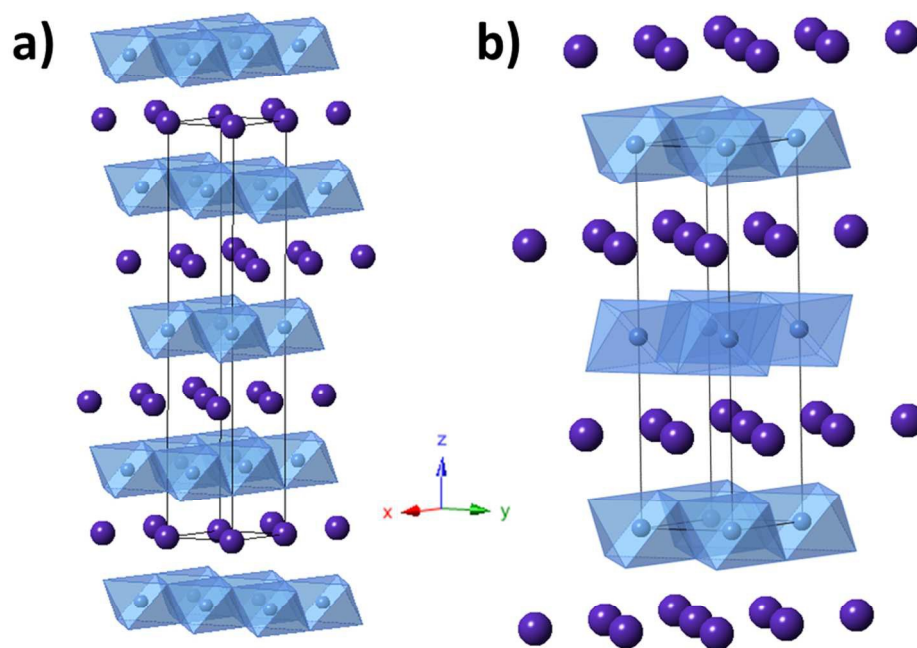
418x320mm (72 x 72 DPI)



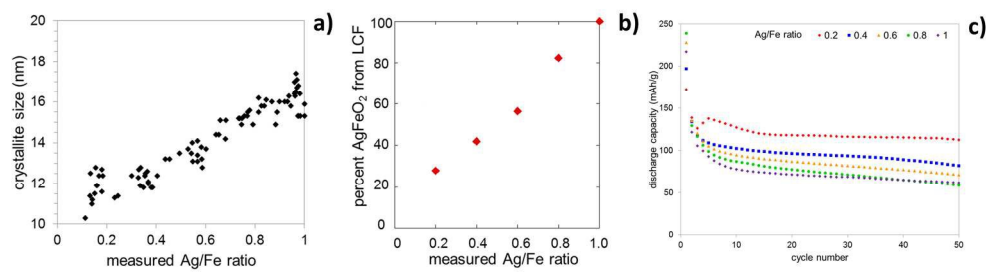
334x387mm (72 x 72 DPI)



482x378mm (72 x 72 DPI)



375x277mm (72 x 72 DPI)



753x208mm (72 x 72 DPI)